JGR Space Physics

RESEARCH ARTICLE
10.1029/2019JA026927

Estimating the Azimuthal Mode Structure of ULF Waves Based on Multiple GOES Satellite Observations

Mohammad Barani[1], Weichao Tu[1], Theodore Sarris[2], Kevin Pham[1,3], and Rob J. Redmon[4]

[1]Department of Physics and Astronomy, West Virginia University, Morgantown, WV, USA, [2]Department of Electrical Engineering, Democritus University of Thrace, Xanthi, Greece, [3]High Altitude Observatory, National Center for Atmospheric Research, Boulder, CO, USA, [4]National Centers for Environmental Information, National Oceanic and Atmospheric Administration, Boulder, CO, USA

Key Points:
- Allowing for both positive and negative mode numbers is important to achieve a realistic mode estimation for ULF waves
- Low-mode ULF waves are less global in MLT coverage than previously assumed, while high-mode waves are more global than assumed
- A cross-pair analysis is performed to reduce the $2n\pi$ ambiguity in the mode number estimation

Correspondence to:
M. Barani,
mobarani@mix.wvu.edu

Citation:
Barani, M., Tu, W., Sarris, T., Pham, K., & Redmon, R. J. (2019). Estimating the azimuthal mode structure of ULF waves based on multiple GOES satellite observations. *Journal of Geophysical Research: Space Physics*, *124*, 5009–5026. https://doi.org/10.1029/2019JA026927

Received 14 MAY 2019
Accepted 10 JUL 2019
Accepted article online 17 JUL 2019
Published online 30 JUL 2019
Corrected 5 MAY 2022

This article was corrected on 5 MAY 2022. See the end of the full text for details.

Abstract Characterizing the azimuthal mode number, m, of ultralow-frequency (ULF) waves is necessary for calculating radial diffusion of radiation belt electrons. A cross-spectral technique is applied to the compressional Pc5 ULF waves observed by multiple pairs of GOES satellites to estimate the azimuthal mode structure during the 28-31 May 2010 storm. We find that allowing for both positive and negative m is important to achieve a more realistic distribution of mode numbers and to resolve wave propagation direction. During the storm commencement when the solar wind dynamic pressure is high, ULF wave power is found to dominate at low-mode numbers. An interesting change of sign in m occurred around noon, which is consistent with the driving of ULF waves by solar wind buffeting around noon, creating antisunward wave propagation. The low-mode ULF waves are also found to have a less global coverage in magnetic local time than previously assumed. In contrast, during the storm main phase and early recovery phase when the solar wind dynamic pressure is low and the auroral electrojet index is high, wave power is shown to be distributed over all modes from low to high. The high-mode waves are found to cover a wider range of magnetic local time than what was previously assumed. Furthermore, to reduce the $2n\pi$ ambiguity in resolving m, a cross-pair analysis is performed on satellite field measurements for the first time, which is demonstrated to be effective in generating more reliable mode structure of ULF waves during high auroral electrojet periods.

1. Introduction

Radial diffusion plays an important role in the transport, acceleration, and loss of energetic electrons in the Earth's radiation belts (Fälthammar, 1965; Kellogg, 1959; Schulz & Lanzerotti, 1974). Therefore, understanding and physically quantifying the radial diffusion process are critical in modeling the complex dynamics of radiation belt electrons. The third adiabatic invariant of electrons, which is inversely proportional to the Roederer L (Roederer, 1970), is violated in radial diffusion. The effects of radial diffusion can be quantified by the coefficient D_{LL}, defined as $D_{LL} = \langle(\Delta L)^2\rangle/2\tau$, which represents the mean-square-displacement of L value for a large number of particles over a time scale τ much longer than the particles' drift period. Enhanced radial diffusion is a result of the drift-resonant interactions between radiation belt electrons and large-scale fluctuations of the magnetosphere's magnetic and electric fields with frequencies comparable to the electrons' drift frequencies (Schulz & Lanzerotti, 1974). Since the drift frequencies of MeV electrons in the outer radiation belt are on the order of MHz, ultralow-frequency (ULF) waves in the Pc5 range (2–7 MHz; Kivelson & Russel, 1995) are most effective in driving radial diffusion. Specifically, the drift resonance condition follows $\omega = m\Omega_D$, where ω is the wave frequency, Ω_D is the electron drift frequency, and m is the azimuthal mode number (or wave number) of ULF waves, which represents (for simple harmonic behavior) the number of wavelengths in the azimuthal direction around the Earth. Characterizing and estimating the azimuthal mode structure of ULF waves are required for calculating the D_{LL} of radiation belt electrons.

Despite its crucial importance, physical quantification of the azimuthal mode number of ULF waves is difficult and has been a missing part in the calculation of the radial diffusion coefficients (e.g., Tu et al., 2012; Sarris, 2014; Sarris & Li, 2017). In principle, to determine the mode structure of a simple harmonic wave at a given frequency up to mode number $m_{\max}$, we need at least $2m_{\max}$ equally spaced azimuthal coherent field measurements. This is hard to achieve from in situ measurements in space due to

insufficient satellite coverage. Arrays of longitudinally separated ground magnetometers offer much better coverage and have also been used for mode number estimation (Chisham & Mann, 1999). However, for high m values, significant amplitude attenuation is expected for ULF waves propagating down to the ground due to the ionospheric screening effect (James et al., 2013; Nishida, 1978), which imposes an extra limitation in resolving physical m values of ULF waves from ground measurements. Due to the difficulties in resolving the actual mode structure of ULF waves, simplified assumptions have been made in previous estimations of the radial diffusion coefficients. For example, in Brautigam et al. (2005), Fei et al. (2006), and Ali et al. (2015) and many previous analyses of D_{LL}, the power of ULF waves was assumed to originate from only $m = 1$. Perry et al. (2005) simulated the effect of ULF waves on the guiding centers of particles through a 3-D model by assuming the waves possessing only $m = 2$. These simplified assumptions of ULF wave mode structure can lead to significant uncertainties in the D_{LL} estimation (e.g., Li et al., 2017; Sarris et al., 2006; Tu et al., 2012). For example, Tu et al. (2012) calculated the D_{LL} of MeV electrons based on ULF waves from global magnetohydrodynamic (MHD) simulation and found that assuming all the power comes from $m = 1$ generally underestimates the total D_{LL}, sometimes by more than an order of magnitude due to the non-power-law spectral shape of the electric field. Therefore, a better quantification of the ULF mode structure is critical.

There are three main approaches to estimating the mode number of ULF waves: (1) performing the cross-phase analysis on pairs of real-time ULF wave measurements (e.g., Le et al., 2017; Loto'aniu et al., 2006; Murphy et al., 2018Olson & Rostoker, 1978; Sarris & Li, 2017; Sarris et al., 2009; Takahashi et al., 2013, 2018), (2) analyzing particle flux observations of particles that are in resonance with the concurrent ULF waves and estimating the mode number based on the drift resonance or drift-bounce resonance condition (e.g., Mann et al., 1998; Takahashi et al., 1990; Zong et al., 2007), and (3) directly calculating the mode spectrum using the global ULF fields from MHD simulations of the magnetosphere (e.g., Fei et al., 2006; Li et al., 2017; Tu et al., 2012). The fundamental difference between the first and the third approaches is that the third approach directly performs Fourier transforms on the discrete signals located at different azimuthal angles covering the full globe (2π), which obeys the Nyquist sampling theorem, while the first approach is applied to a pair of time signals that are azimuthally separated and observing the same ULF wave, which does not obey the Nyquist theorem. In other words, if the azimuthal separation between the pair of field measurements is $\Delta\lambda$ in degrees, the m resolved using the first approach is determined by the ratio between the phase difference between the two signals and $\Delta\lambda$ which will be discussed in detail in section 3, while in the third approach the resolved m cannot go over the Nyquist limit, which is half of $360°/\Delta\lambda$. Zong et al. (2017) provided a comprehensive review on recent works in calculating the m values using the first two data-driven approaches. Shi et al. (2018) also provided a table of comparisons among some of the recent poloidal ULF wave case studies. Sarris and Li (2017) performed cross-spectral and cross-phase calculations to three azimuthally aligned GOES magnetometer data to obtain the mode structure of ULF waves during two storm periods. They found that lower geomagnetic activity (weaker Dst) generally favors the distribution of power in primarily low m numbers, whereas intense geomagnetic activity favors a more even distribution of power across all resolved m numbers. In studying the ULF modulation of energetic particles observed by CLUSTER satellite, Zong et al. (2007) estimated $m \leq 10$ for toroidal ULF waves based on the drift resonance condition. Tu et al. (2012) calculated the full mode structure of ULF waves by performing FFT analysis on the global MHD fields generated by the Lyon-Fedder-Mobarry MHD code. They found that the power of the compressional ULF waves in $m = 1$ mode is related primarily to solar wind dynamic pressure variations, while power in $m > 1$ is related primarily to the nightside substorm activity.

Even though significant progress has been made in quantifying the mode number of ULF waves, when applying the mode number results to calculations of radial diffusion coefficients, two aspects of the mode structure are usually oversimplified. First, some of the methods mentioned above using the cross-phase techniques (e.g., Sarris & Li, 2017) or global MHD simulations (e.g., Tu et al., 2012) assumed only positive m values for the ULF waves, whereas in reality the mode number can be either positive or negative corresponding to the waves propagating in either eastward or westward direction (e.g., Chisham & Mann, 1999; Murphy et al., 2018; Yeoman et al., 2010). This assumption will lead to uncertainty in D_{LL} quantification since only positive-mode ULF waves would resonate with radiation belt electrons, which drift eastward. Therefore, when assuming $m > 0$, the resulting D_{LL} could overestimate the real D_{LL} and should only be considered as an upper limit. Second, in many of the previous calculations of D_{LL}, the resolved mode structure of

ULF waves was usually assumed to be global around the Earth, which may not always be an accurate assumption. For example, through ionospheric radar observations, Fenrich et al. (1995) found that $m > 17$ ULF waves are concentrated in the midnight and local afternoon, while $m < 17$ waves are concentrated near the flank regions. Similarly, Sarris and Li (2017) found that the mode number values of Pc5 ULF waves are generally higher at the nightside than the dayside. Therefore, assuming a uniform mode structure around the Earth in radial diffusion calculations, rather than using a realistic local time distribution of the mode number, can lead to significant uncertainty in D_{LL} estimation where the local time dependent mode structure needs to be properly drift averaged. In summary, a reliable estimate of the diffusion coefficients requires including both the positive and negative mode numbers of ULF waves, as well as specifying the local time coverage of the specific mode structure, the calculation of which is the subject of the work presented herein.

In this paper we quantify the azimuthal mode structure of the compressional Pc5 ULF waves observed by multiple pairs of GOES satellites during the 28-31 May 2010 geomagnetic storm. Even though compressional (B_z), poloidal (E_φ), and toroidal (E_r) mode ULF waves can all lead to radial diffusion of energetic particles in realistic geomagnetic field (e.g., Elkington et al., 1999, 2003; Fälthammar, 1965; Mann et al., 2013), here we only focus on the compressional mode since GOES only measures magnetic field but not electric field. We apply the cross-spectral technique used in Sarris (2014) and Sarris and Li (2017), but using up to five GOES satellites available during the event to better address the limitations in the previous mode number calculations mentioned above. The five GOES satellites cover a wide range of local times at the same time, which provides an excellent opportunity to more reliably estimate temporal and spatial variations of mode numbers, as well as to resolve the local time extent of the mode structure. Both positive and negative mode numbers are included in our calculation, and the availability of multiple overlapping pairs of satellites enables a comparative analysis to reduce the $2n\pi$ ambiguity in the phase difference and mode number calculation, which is performed here for the first time for ULF wave measurements in space. The paper is organized as follows: Section 2 introduces the 28-31 May 2010 storm with its corresponding solar wind and geomagnetic conditions, the cross-wavelet transform (XWT) method is described in section 3, the results from our analysis of the 28-31 May 2010 storm regarding the mode structure are discussed in section 4, validation work to reduce the $2n\pi$ ambiguity in the mode estimation is discussed in section 5, and discussions and conclusions are included in section 6.

2. 28-31 May 2010 Storm Event

For the period of 28-31 May 2010, we analyze the compressional Pc5 ULF magnetic pulsations using in situ GOES magnetometer measurements. The geomagnetic indices and solar wind parameters are shown in Figure 1. A small interplanetary shock arrived at the Earth at ~03UT on 28 May; subsequently, a long storm commencement was observed, from ~03 to ~21UT on 28 May. The solar wind dynamic pressure (P_{dyn}) remained high following the shock and interplanetary magnetic field (IMF) B_z turned southward and then northward twice during the storm commencement period. During the main phase of the storm, from ~21UT on 28 May to ~12UT on 29 May, the IMF B_z turned southward and stayed southward over the entire storm main phase. The auroral electrojet (AE) index increased during the main phase and reached its maximum value at the end of the main phase. The storm then continued with a long recovery phase. During the early recovery phase (~12-19UT on 29 May), AE remained high but started to drop and the southward IMF B_z started to decrease as well. Then in the late recovery phase, the AE index exhibited strong fluctuations with elevated activity during many intervals. The IMF B_z also fluctuated between southward and northward during the late recovery phase with the solar wind flow speed increasing gradually. In fact, the late recovery phase continued for a couple of days after 31 May until another storm occurred (not shown in Figure 1).

The 28-31 May 2010 storm event is chosen in this mode number estimation study for three reasons. First, we have exceptional GOES data coverage during this interval, as the magnetometer data from five GOES satellites are available, which is ideal for mode number calculations. Figure 2a depicts the locations of the five GOES satellites (GOES 11, 12, 13, 14, and 15) in the geocentric solar equatorial coordinate system at 11UT of 28 May. The averaged west longitudes of these satellites during 28 May are listed in Figure 2b, and the azimuthal spacings between the satellites are relatively fixed during the entire storm interval. Based on Figure 2, we see the azimuthal separation of every two adjacent GOES satellites is ~15°, except for GOES 11 and GOES 14, which are separated by ~31°. In the next section we will see that a close azimuthal

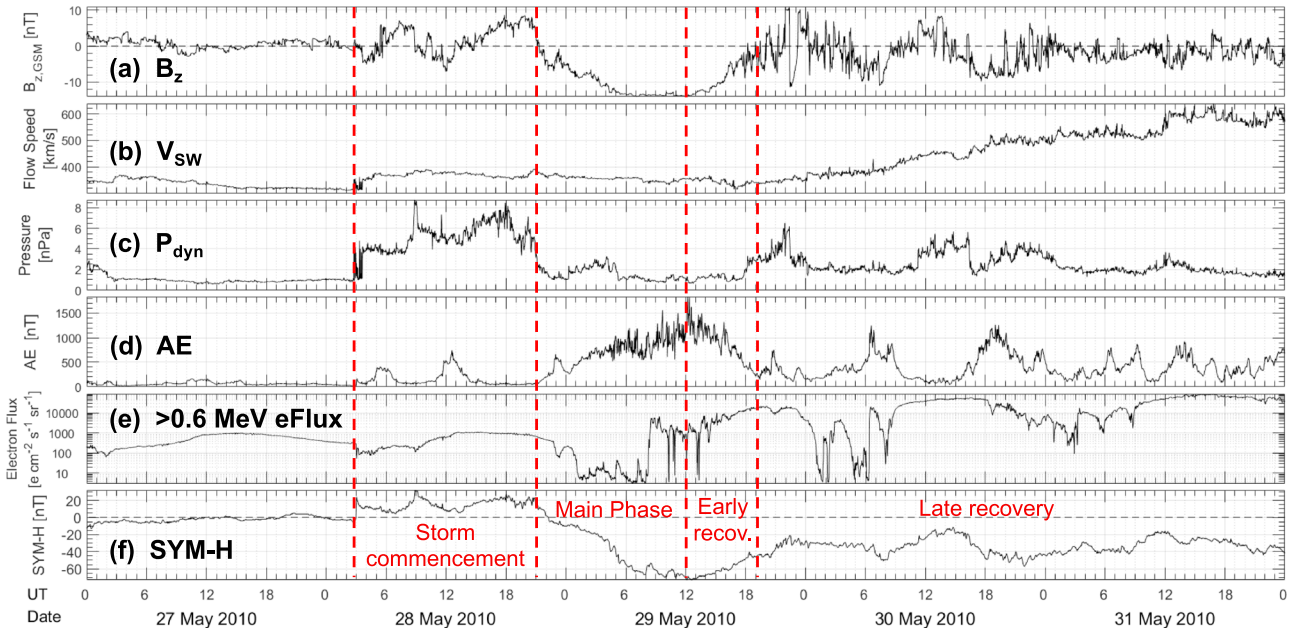

Figure 1. (a–f) The geomagnetic indices and solar wind parameters during the 27-31 May 2010 storm based on the OMNI data set, including IMF B_z, total bulk solar wind flow speed V_{SW}, solar wind dynamic pressure P_{dyn}, AE index, and SYM-H index. The flux of >0.6-MeV electrons measured by the GOES 13 satellite is shown in panel (e).

separation of ~15° can resolve azimuthal mode numbers ranging from -12 to 12. In addition, the five satellites span a wide range of magnetic local times (MLTs) at each UT, which is useful to specify the local time extent of the mode structure. The second reason this event is selected is its distinct periods with either dominant solar wind dynamic pressure or AE activity. Based on Figure 1, we see that during the

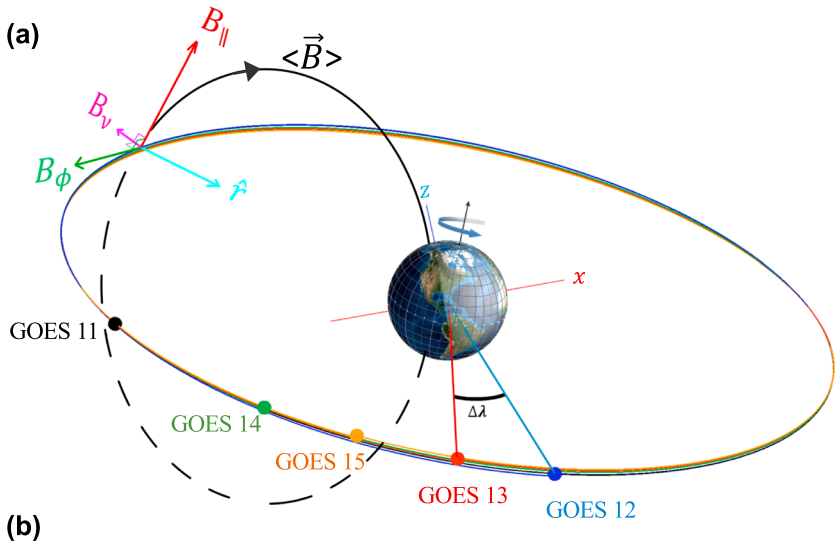

(b)

West longitude	59.9°	74.8°	89.8°	104.5°	135.5°

Figure 2. (a) Schematic of the locations of five GOES satellites in geocentric solar equatorial coordinate at 11UT of 28 May 2010, with $\Delta\lambda$ denoting the azimuthal separation between GOES 13 and 12. The magnetic field perturbations on top of ambient magnetic field $<\vec{B}>$ are decomposed into three components: $B_{||}$ compressional, B_{ν} poloidal, and B_{ϕ} toroidal. (b) Averaged west longitude (λ) of the five GOES satellites during 28 May 2010.

storm commencement, the solar wind dynamic pressure increased to a high level, while the AE index stayed low, except for two small enhancements. In contrast, during the storm main phase and early recovery phase, the solar wind dynamic pressure dropped to a very low level, while the AE index became very active (up to around 1,800 nT). Previous studies have shown that AE and solar wind P_{dyn} are correlated with different ULF mode structures (e.g., Tu et al., 2012). For instance, by analyzing the mode structure of compressional B_z field from the LFM MHD simulation of a CIR storm in March 2008, Tu et al. (2012) showed that the power of B_z at $m = 1$ is generally correlated with the solar wind P_{dyn}, while the $m > 1$ power is mostly enhanced when the AE index is high. The distinct periods of high P_{dyn} vs. high AE during our selected event provide a unique opportunity to examine how different patterns of AE and solar wind dynamic pressure affect the mode structure of ULF waves. Lastly, the event is chosen due to the concurrent enhancement of MeV electron flux. Figure 1e plots the flux of >0.6-MeV electrons measured by GOES 13, which shows a fast drop during the early main phase followed by a significant increase near the end of the main phase. To study the role of radial diffusion to the observed enhancement of MeV electrons, accurate estimation of the ULF wave mode number is required which further motivates this work.

3. The XWT Method

To estimate the azimuthal mode structure of ULF waves, here we apply the XWT method developed in Sarris et al. (2013) and Sarris (2014). Wavelet analysis is a technique that is increasingly used due to its profound advantages over the conventional methods (such as Fourier analysis); for example, it can better resolve the spectral analysis for nonstationary signals and in low-frequency regimes, and XWT provides a precise correlation between two signals while analyzing their phase-shifted, equi-wavelength values (Eriksson, 1998; Rioul & Vetterli, 1991). The Morlet wavelet transform is used in our spectral analysis (Eriksson, 1998; Grinsted et al., 2004; Torrence & Compo, 1998), and more details about the XWT technique can be found in Sarris et al. (2013) and Sarris (2014). Here we briefly discuss how to use the XWT method to estimate the ULF wave mode number. If we have two magnetic field wave signals measured by two GOES satellites that are azimuthally separated by $\Delta\lambda$ (e.g., between GOES 12 and 13 in Figure 2), performing XWT on the pair of signals provides X-Phase values, which are the phase differences between the two signals, and X-PSD values, which are the cross power spectral density (PSD) values. The results include one set of (X-Phase, X-PSD) values for each time and frequency. Then the azimuthal wavenumber (mode number) can be calculated as

$$m = \mathrm{X{-}Phase}/\Delta\lambda \tag{1}$$

One major assumption of using the XWT method to resolve the mode number is the good correlation between the two signals. Therefore, to ensure that the mode number results are reliable, for the selected time interval of the analysis, we only include the XWT results with X-PSD values higher than the minimum value by at least x% multiplied by (maximum − minimum; Sarris et al., 2013). This method works to select the correlated and high-amplitude signals from both satellites and to exclude the low-amplitude signals from both satellites that are below a certain low signal level. Although the less correlated signals with one at high amplitude and the other at low amplitude could still be included in the results, fortunately, this is not the case for our event for which the coherence between the two signals is very high (see detailed results in section 4). Additionally, this method must be applied carefully if the X-PSD from both satellites is at a low level, which is not the case for our event as the storm time ULF wave power is generally high. The high coherence grants the use of a certain X-PSD percentage threshold to select the relatively high amplitude and correlated signals. The value of $x = 0.1$ was selected here based on visual inspection and testing of the correlations between the two observed signals. It is lower than the percentage value used in previous works (e.g., Sarris, 2014; Sarris et al., 2013) due to the higher correlation between the two observed signals in our event. We have also tested the results with different values of x, and there are no significant changes in our conclusions. Since the XWT method only resolves the trigonometric values of the phase difference between the two signals, the resulting X-Phase has a so-called $2n\pi$ ambiguity, which leads to uncertainty in the mode number estimation. First, the $2n\pi$ ambiguity can affect the sign of the mode number. The X-Phase from the XWT analysis can be either constrained to be positive only, that is, in the range of [0°, 360°] or to include both positive and negative values, that is, in the range of [-180°, 180°]. Many previous

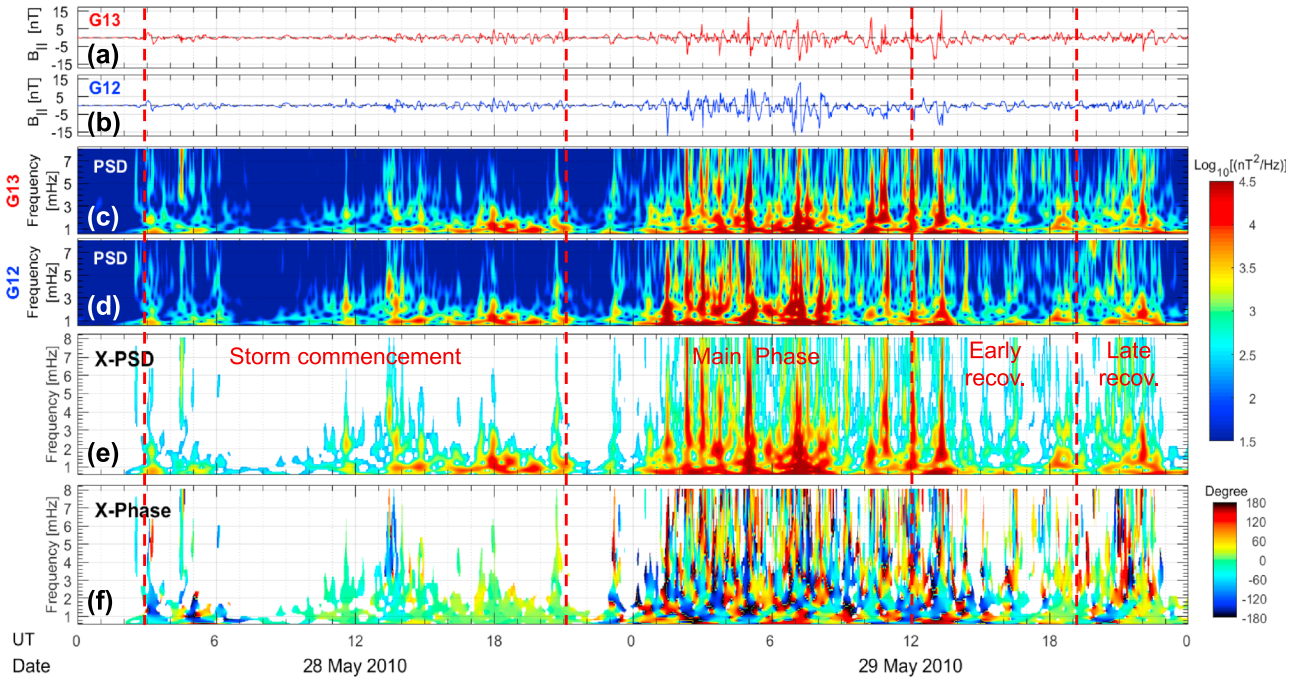

Figure 3. (a and b) Time series of the measured compressional magnetic field pulsations by GOES13 (G13) and GOES12 (G12) over 28-29 May 2010. (c and d) The calculated Power Spectral densities (PSD) vs. frequency and time for the pair of satellites. (e and f) Calculated cross power spectral density (X-PSD) and cross phase difference (X-Phase) between the two signals using cross-wavelet transform analysis. A threshold of 0.1% of minimum-to-maximum power above the minimum has been applied to X-PSD to exclude the low X-PSD values.

applications of the XWT and cross-spectrogram Fourier analyses (e.g., Li et al., 2016; Sarris, 2014; Sarris & Li, 2017; Sarris et al., 2013) assumed only positive X-Phase (or mode number), which corresponds to eastward propagating ULF waves that can drift-resonate with radiation belt electrons. However, waves can propagate in both directions so here we also include negative mode numbers (i.e., X-Phase in the range of [-180°, 180°] in section 4) to incorporate both eastward and westward propagating waves. This is similar to the studies in Chisham and Mann (1999) and Murphy et al. (2018) using ground-based and in-situ magnetometer data and the Super Dual Auroral Radar Network studies in Yeoman et al. (2010). Second, the $2n\pi$ ambiguity suggests that the X-Phase cannot be uniquely determined since we do not know how many full wave periods are in between the two measurements. However, this ambiguity can be largely reduced by validating the mode number results between two pairs of signals that overlap azimuthally, which will be carried out in section 5.

4. The Mode Number Estimation Results

The XWT technique is applied to multiple pairs of GOES magnetometer data to estimate the azimuthal mode structure of the compressional-mode ULF waves during the 28-31 May 2010 storm. Magnetic field measurements with 1-min cadence from the four closely spaced GOES magnetometers are used in the analysis, which are GOES 14, 15, 13, and 12, located as shown in Figure 2. The azimuthal separation between every two neighboring satellites is about 15°, which means that we can resolve the mode number in range of [-12, 12] considering X-Phase range of [-180°, 180°] from the XWT analysis and equation (1) for mode estimation. To obtain the compressional component of the ULF waves, we first project the magnetic field measurements to a mean field-aligned coordinate system as in Sarris et al. (2013; which is based on the averaged field over a 30-min time window as the ambient field). Then, after subtracting the 30-min window-averaged baseline fields, the remaining fluctuating magnetic fields are decomposed into compressional, poloidal, and toroidal components, denoted as $B_{||}$, B_{ν}, and B_{ϕ}, respectively, in Figure 2a.

The $B_{||}$ components of the magnetic field pulsations measured by GOES 12 and 13 during the first 2 days of May 2010 storm are plotted in Figures 3a and 3b, respectively. Their corresponding PSDs, calculated using the wavelet transform, are shown in Figures 3c and 3d. The similarity between the two PSDs suggests

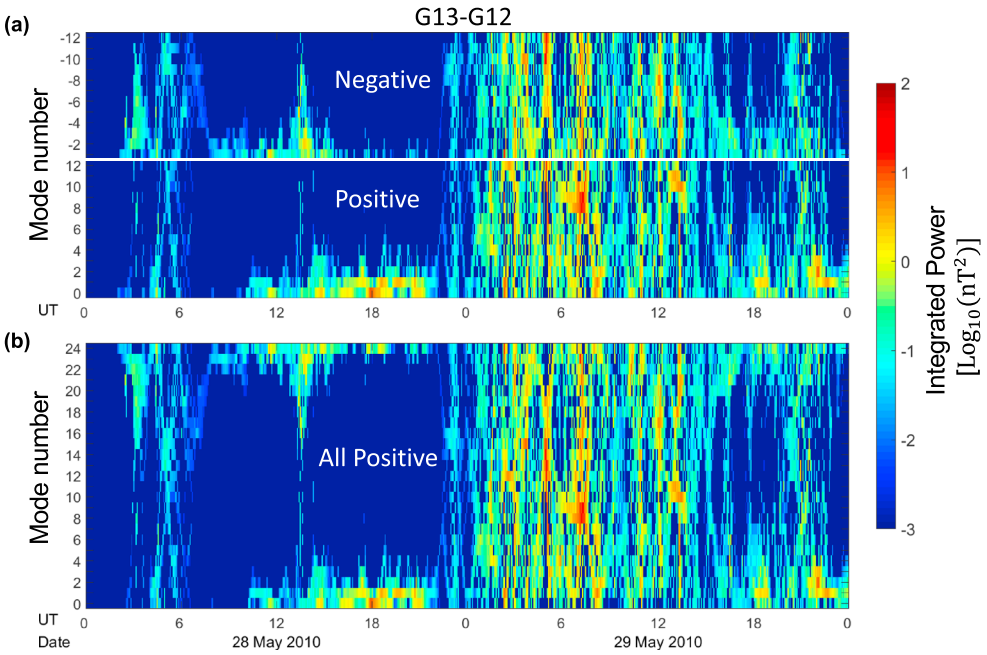

Figure 4. Integrated wave power versus time and mode number based on the cross-wavelet transform analysis of the GOES 13 and 12 pair, by assuming that (a) the mode number can be both positive and negative or (b) the mode number can only be positive.

strong correlation between the two signals, which support the use of the XWT method. After performing the XWT analysis on the GOES 13 and 12 pair of signals, Figure 3e illustrates the X-PSD vs. frequency and time and Figure 3f illustrates the estimated X-Phase between the two signals in the range [-180°, 180°]. As described above, a threshold of $x = 0.1$ corresponding to 0.1% of the minimum-to-maximum difference above the minimum power has been applied on the X-PSD to exclude the frequency-time regimes with low common power (low coherence) between the two signals, which are the blank regions in Figures 3e and 3f. The results show stronger power of Pc5 ULF waves covering a wider range of frequencies during 29 May (which includes the storm main phase and recovery phase) than 28 May (which includes the storm commencement). In addition, the X-Phase values and distributions are very different between the two days, which suggests distinct features in the ULF wave mode structure.

To estimate the mode numbers, equation (1) is used to compare the X-Phase in Figure 3f with the azimuthal separation $\Delta\lambda$ between GOES 13 and GOES 12 (which is ~15° from Figure 2). The nearest integer is used in the m estimation, which means in general the positive mode number of $+|m|$corresponds to X-Phase in the range of $\left(\frac{2m-1}{2}\Delta\lambda, \frac{2m+1}{2}\Delta\lambda\right)$, and the negative mode $-|m|$ corresponds to X-Phase in the range of $\left(-\frac{2m+1}{2}\Delta\lambda, -\frac{2m-1}{2}\Delta\lambda\right)$. Note here we assume that the uncertainty in m estimation is <0.5, which is consistent with previous works (e.g., Sarris, 2014; Sarris et al., 2013). However, accurately quantifying the uncertainty in m using equation (1) requires estimation of the uncertainty in X-phase from the XWT analysis and the uncertainty in $\Delta\lambda$ (which is almost negligible in our case), which will be pursued in a future effort. Based on this method, the m number at each time and frequency is estimated using the X-Phase in Figure 3f with Figure 3e showing the corresponding X-PSD at each mode. Then to achieve the total wave power at different mode numbers, we sum the X-PSD values corresponding to the same mode number for each time and plot the integrated-over-frequency wave power versus time and mode number in Figure 4. In this analysis, we define the X-Phase to be in the range of [-180°, 180°]; thus, the resolved m range is [-12,12] as shown in Figure 4a with the power distribution for the negative modes plotted on the top and the distribution for the positive modes plotted underneath. We see that during the first day, 28 May, the wave power is mostly dominant at low-mode numbers (both negative and positive), while for the second day, 29 May, the power is almost evenly distributed across all different modes from low to high. In contrast, if we only allow positive mode numbers, similar to previous studies in D_{LL} calculations, the X-Phase will be defined in the range of [0°, 360°] and the resolved m range is [0,24] with results shown in Figure 4b. We notice that the wave power in the low negative

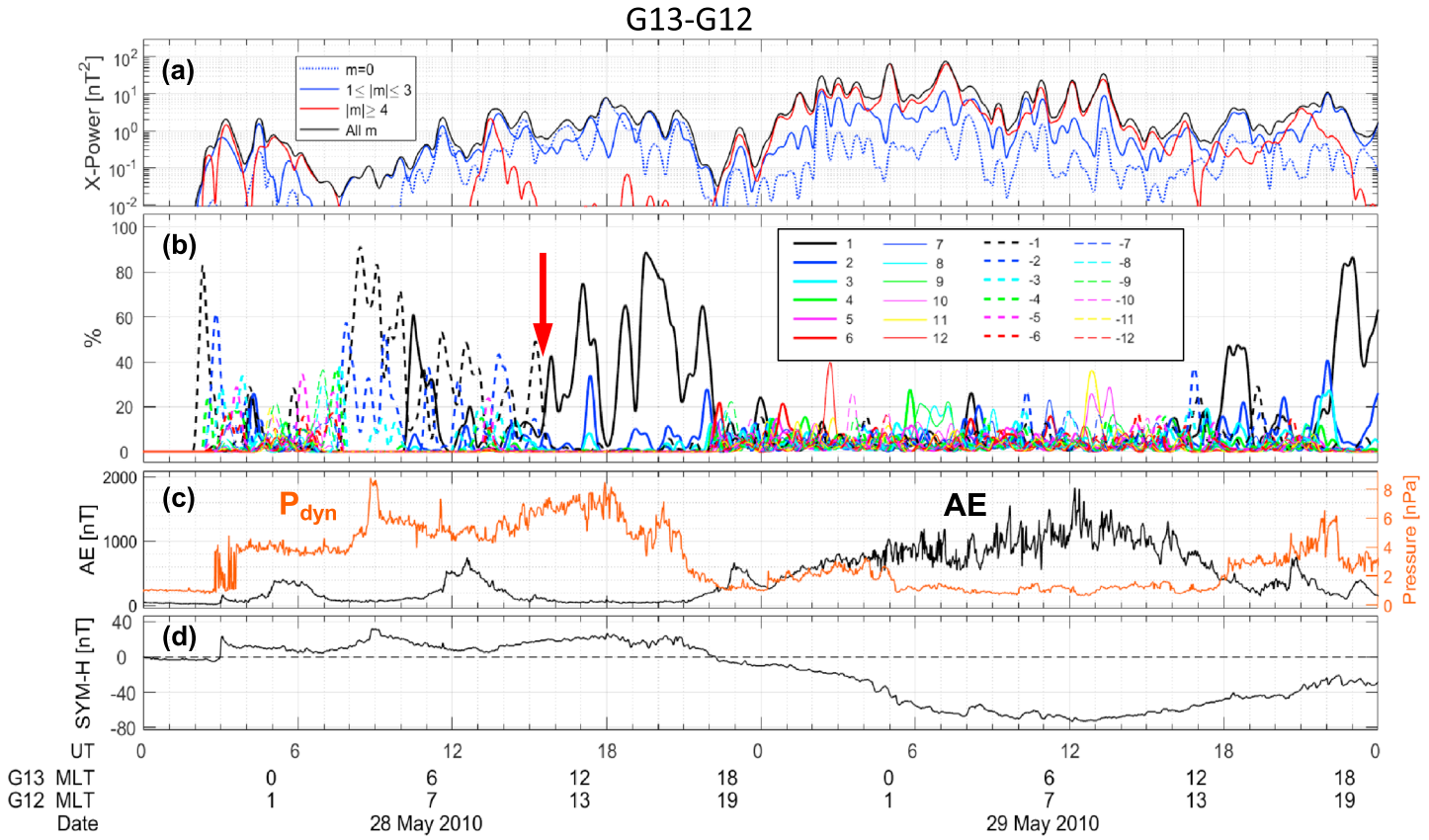

Figure 5. Mode number distribution based on the cross-wavelet transform analysis of the GOES 13 and 12 pair: (a) Integrated wave power for low mode ($1 \leq |m| \leq 3$, blue curve), high mode ($|m| \geq 4$ up to 12, red curve), zero mode ($m = 0$, blue dotted curve), and all mode numbers ($|m| \leq 12$ including $m = 0$, black curve). (b) Fraction of the power embedded in each mode number from -12 to 12. (c) Solar wind dynamic pressure P_{dyn} and AE index. and (d) SYM/H index.

modes in Figure 4a is basically mirrored to the power in high positive modes in Figure 4 due to the different assumptions of the X-Phase range (adding 2π to X-Phase or adding 24 to m based on the 15° azimuthal separation between satellites, thus $m = -1$ flipping to $m = 23$, $m = -2$ flipping to $m = 22$, etc.). There are two subtle exceptions due to the edging effect: $m = 0$ corresponds to X-Phase in the range of $(-0.5\Delta\lambda, 0.5\Delta\lambda)$ for the "positive and negative" case in Figure 4a. Converting to the "all positive" case in Figure 4b, the $m = 0$ X-Phase would be in the range of $(23.5\Delta\lambda, 24\Delta\lambda)$ for the negative half after adding 2π but stay unchanged in the range of $(0°, 0.5\Delta\lambda)$ for the positive half. The former now corresponds to $m = 24$ in the all positive case and the latter corresponds to $m = 0$. Therefore, the $m = 0$ X-PSD in the positive and negative case splits into the $m = 0$ and $m = 24$ X-PSD in the all positive case. Similarly, the $m = 12$ X-PSD in the all positive case corresponds to the sum of the $m = 12$ and $m = -12$ X-PSD in the positive and negative case. Comparing the results in Figures 4a and 4) and considering the nature of ULF pulsations, the wave power is not expected to be higher at higher modes than at lower modes, especially during the period of high solar wind dynamic pressure (e.g., 28 May) when the pulsations are at large scales. Therefore, the power versus mode number distribution during the first day in Figure 4b by assuming all positive modes seems unrealistic, while the distribution becomes more realistic when allowing for both positive and negative modes, as shown in Figure 4a. However, this reasoning cannot be applied to the second day, when the power is almost evenly distributed over all modes. Here we define the X-Phase range to be [-180°, 180°] to allow for both positive and negative modes for both days but leaving the detailed work of reducing the $2n\pi$ ambiguity during the second day (high AE period) in section 5.

To further investigate the mode distribution of ULF waves, we calculate the integrated wave power for zero (m=0), low ($1 \leq |m| \leq 3$), high ($4 \leq |m| \leq 12$), and all ($|m| \leq 12$ including $m = 0$) mode numbers and plot the results in Figure 5a. We see that the power in all mode numbers (black curve) is generally correlated with solar wind dynamic pressure, P_{dyn}, during high P_{dyn} times and the AE index during high AE times (plotted

in Figure 5c), and is higher during the active AE period. Note there is an interesting outlier during the P_{dyn} peak at 9 UT of 28 May, which will be discussed later. Again, panel (a) shows that the power at low mode (blue curve) is generally dominant over the high mode (red curve) during 28 May, the high P_{dyn} period. It is interesting to note that the high-mode power (red curve) becomes comparable to or even higher than the low-mode power during 3–8 UT on 28 May when the two GOES satellites are near midnight (see the MLT labels for both satellites in the x axis below UT). The power in higher mode numbers also shows a temporary increase during 13-15UT when the AE level is elevated during the high P_{dyn} day (28 May). Then during the high AE and low P_{dyn} period (29 May 0-17UT), the power at high mode stays comparable or even higher than low mode. We also calculated the fraction of total power embedded in each mode number and plot its variation in Figure 5b. For the high P_{dyn} period during 28 May, we see that the mode numbers at $m = 1$ (solid black curve) and $m = -1$ (dashed black curve) generally dominate over other modes. One interesting feature we find is that the sign of m starts as generally negative from 5.5UT of 28 May and then changes to positive at 15.5 UT or 10.5 hr MLT (if using the MLT of the trailing satellite of the pair, GOES 13).

Subsequently, we investigate whether the change of sign in m, as marked by a red arrow in Figure 5b, is a temporal or spatial effect. First, based on the solar wind conditions during the high P_{dyn} period of 28 May, we cannot identify any temporal variations of the solar wind drivers that correspond to the pattern and change of the mode number, which indicates that this sign change might not be temporal. To illustrate the spatial dependence, we convert the temporal variation of the mode fraction in Figure 5b to a polar plot in Figure 6a to display the MLT distribution of mode fraction during the high solar wind P_{dyn} period (the day of 28 May). The color and line styles are of the same format as of Figure 5b, and the MLT of the trailing satellite, GOES 13, is used for the plot. There is a clear change of sign in m at around 10.5 hr MLT as denoted by the thick arrows in Figure 6a. To further investigate if the sign change is spatial, we performed the same XWT analysis for another two pairs of GOES satellites and plot the resolved spatial distributions of the mode fraction in Figures 6b and 6c for the same high P_{dyn} period. According to the satellite locations in Figure 2, the GOES 15 and 13 pair passes through the same MLT region an hour later than the GOES 13 and 12 pair, with GOES 14 and 15 pair delayed for one more hour. However, Figure 6 shows that the three satellite pairs observe a sign change in the mode number at around the same MLT region (9.5-10.5h MLT), which suggests that the change of sign is a spatial effect. As discussed earlier, the sign of mode number indicates the propagation direction of the wave: $m > 0$ corresponds to east propagating waves as denoted by the curved arrows in Figure 6, and $m < 0$ means west-propagating waves. The change of the wave propagation direction slightly before noon is consistent with the picture of compressional ULF waves driven by solar wind dynamic pressure variations (e.g., Hughes, 1994; Olson & Rostoker, 1978). The high-pressure solar wind buffets the Earth's magnetosphere near noon and generates ULF waves propagating around the Earth in antisunward directions.

Figure 6 also shows that the MLT distributions of the mode fraction are not identical among all the pairs for the same period. This is due to the fact that the three pairs are located at different MLT sectors at the same time. The MLT coverage from the three pairs can be used to infer the local time extent of the resolved mode structure. For example, based on the x-axis in Figure 5, we see that at ~20UT on 28 May the GOES 13 and 12 pair is located at 15-16 hr MLT (considering that the two satellites are separated by 1 hr in MLT). At the same time, the GOES 15 and 13 pair is at 14-15 hr MLT and the GOES 14 and 15 pair is at 13-14 hr MLT. Figure 6 shows that all three pairs observe a dominant mode at $m = 1$ over all covered MLT regions (13-16 hr), suggesting that the low-mode structure covers at least 3 hr in MLT near the dayside. In contrast, at 9 UT of 28 May when the GOES 13 and 12 pair is located at 04-05 hr MLT (based on Figure 5) and the GOES 15 and 13 pair is at 03-04 hr MLT, Figures 6a and 6b show that both pairs observe dominant low-mode structure at $m = -1$. However, the GOES 14 and 15 pair located at 02-03h MLT concurrently finds the wave power to be evenly distributed among all modes (up to ± 12). Therefore, at this time the low-mode waves are only limited to MLT regions away from the midnight (>3 hr MLT), which suggests that the low-mode ULF wave structure may not be as global as previously assumed in D_{LL} quantification. This also explains the outlier in Figure 5 a. Even though the solar wind P_{dyn} shows a peak at 9 UT of 28 May, the total power, which is dominated by low modes, does not show an increase since the GOES 13 and 12 pair is located near midnight at that time.

The analyses above are for the high solar wind P_{dyn} period. To analyze the high-AE period (29 May 0-17UT), the mode fraction results in Figure 5b shows that the power spreads over all mode numbers from low to high. Similar polar plots illustrating the MLT distribution of the mode structure during the high AE period are

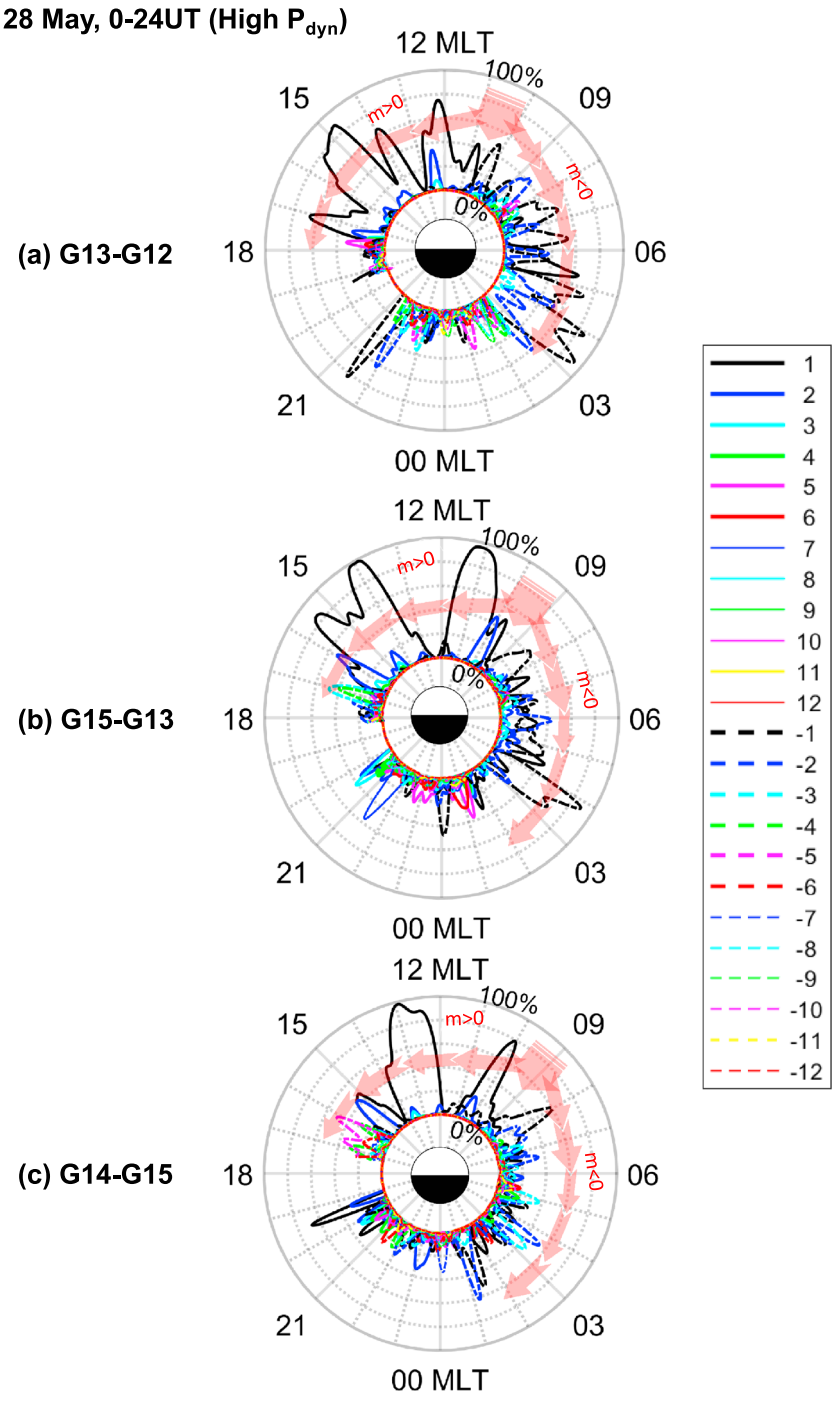

Figure 6. Magnetic local time (MLT) distribution of the power fractions at different mode numbers from the pairs of (a) GOES13 and 12, (b) GOES15 and 13, and (c) GOES14 and 15 during the day of high solar wind dynamic pressure (28 May). The wave propagation direction (or sign of *m*) is denoted by the red arrows.

included in Figure 7. Again, panel (a) corresponds to the same GOES 13 and 12 pair as in Figure 5, while panels (b) and (c) correspond to the other two pairs, GOES 15 and 13 and GOES 14 and 15, which follow the GOES 13 and 12 pair in MLT. The grey sectors in panels (b) and (c) are due to data gaps in the GOES 15 magnetometer data during this period. Figure 7 shows that the evenly distributed power across all modes is consistently observed by all three pairs, which further confirms the resolved mode structure. Furthermore, the results from three pairs show that the MLT coverage of the evenly distributed mode

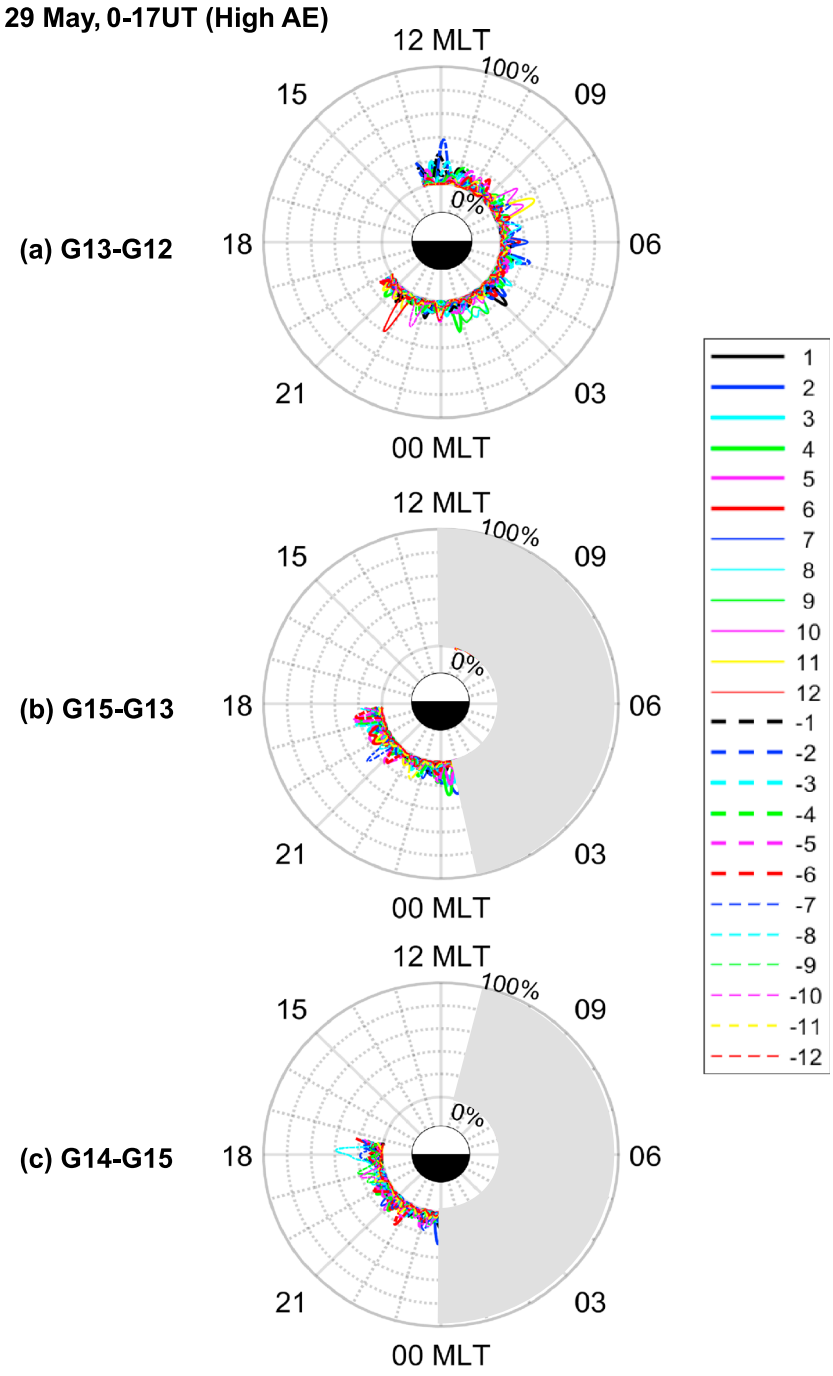

Figure 7. (a–c) The same format as Figure 6 but for the period of high auroral electrojet (AE; 29 May 0-17UT). The grey sectors in (b) and (c) are due to gaps in the GOES 15 magnetometer data.

structure appears to be more global than generally assumed for high AE periods. Significant contribution from high modes is not limited to regions close to the midnight, and it can also cover the MLT regions all the way over to the dayside.

5. Reducing the $2n\pi$ Ambiguities in Mode Number Estimation

In section 3 we discussed the $2n\pi$ ambiguity in the resolved X-phase since the XWT method can only calculate the trigonometric values of the phase differences. The $2n\pi$ ambiguity not only affects the sign of the

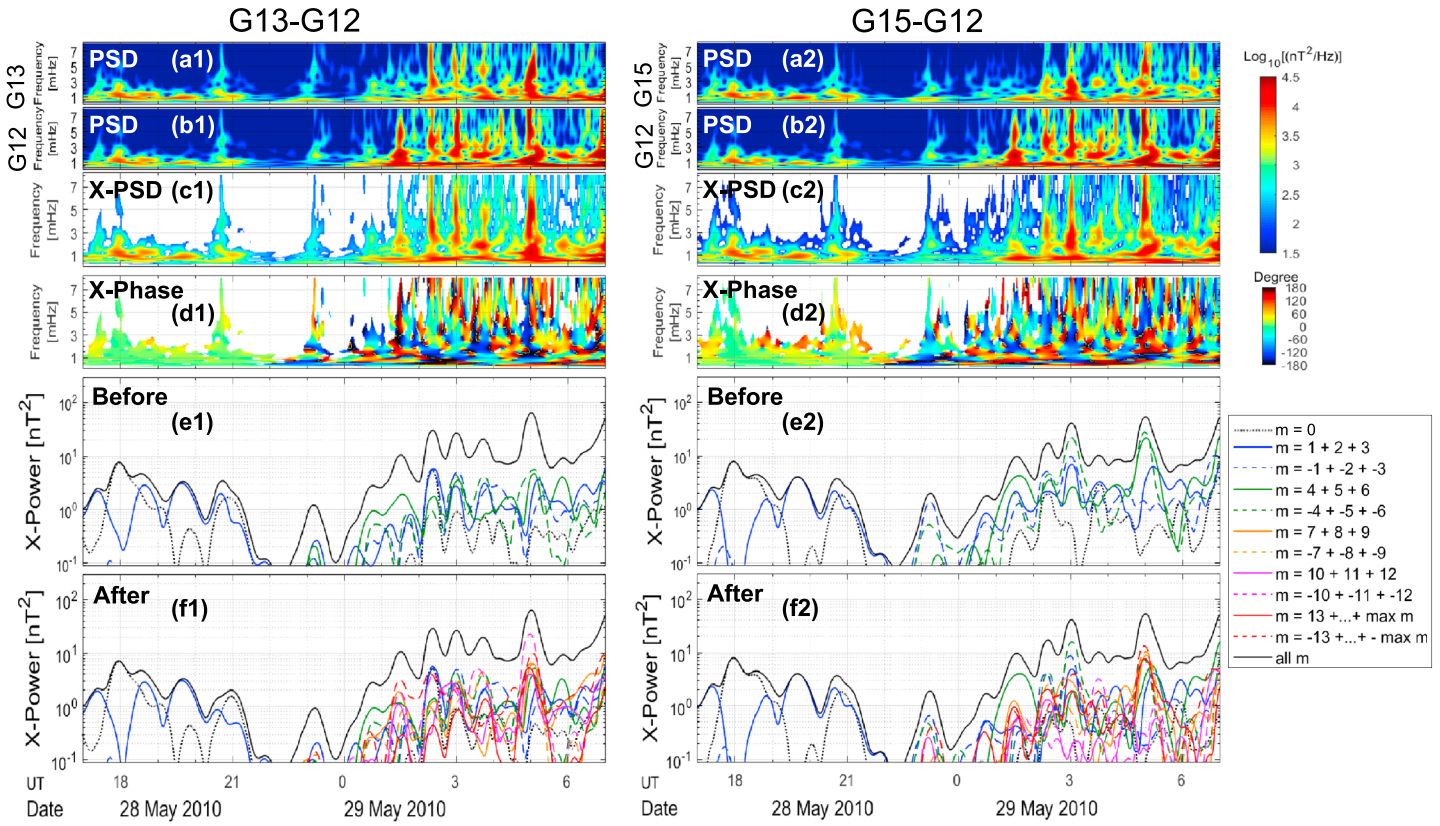

Figure 8. (a1-b1) Power spectral densities (PSD) vs. frequency and time measured by GOES 13 and 12, respectively; (c1-d1) Calculated cross power spectral density (X-PSD) and cross phase difference (X-Phase) for the pair of GOES 13 and 12 using cross-wavelet transform analysis. (e1) Integrated wave power at different mode number ranges plotted in different colors specified in the right legend. (f1) The same as (e1) but after the cross-pair analysis to reduce the $2n\pi$ ambiguity. (a2-f2) The same format as (a1-f1) but for the GOES 15 and 12 pair.

mode number but also leads to uncertainties in the calculated X-phase or mode number, since we do not know how many full wave periods are included in between the two measurement points. For low-mode structure during high solar wind P_{dyn} period, we have already demonstrated in Figure 4 that allowing for both positive and negative modes can lead to more realistic mode structure. To further reduce the $2n\pi$ ambiguity in the resolved X-Phase, especially for the high AE period, here we perform a cross-pair analysis to compare and reconcile the mode number results from two pairs of signals that overlap azimuthally.

Specifically, the two overlapping pairs of GOES 13 and 12 and GOES 15 and 12 are used in this analysis. As shown in Figure 2, both pairs cover the MLT region between GOES 13 and 12, with the GOES 13 and 12 pair separated by 1 hr in MLT and the GOES 15 and 12 pair separated by 2 hr in MLT. For the pair of GOES 13 and 12, Figures 8a1 and 8b1 show the PSDs measured by GOES 13 and 12, respectively, and Figures 8c1 and 8d1 illustrate the resolved X-PSD and X-Phase using the XWT analysis. Figures 8a2–8d2 show the same results for the GOES 15 and 12 pair. The time period from 17UT of 28 May to 7UT of 29 May is selected for this analysis since it includes a high P_{dyn}-low AE interval (17 to 22UT of 28 May) followed by a low P_{dyn}-high AE interval (22UT of 28 May to 7UT of 29 May) as shown in Figure 9c. The similarity of X-PSD between the two pairs, as shown in panels (c1) and (c2) of Figure 8, demonstrates that the two pairs are likely measuring the same ULF pulsations during that time. Based on the X-PSD and X-Phase values, panels (e1) and (e2) show the integrated wave power at different mode number ranges for the two pairs. Since the azimuthal separation between the GOES 13 and 12 pair is ~15° and the X-Phase is defined to be in the range of [-180°, 180°], the resolved m range is [-12, 12] in panel (e1), with different colors and line styles showing power in different mode ranges, as indicated in the legend on the right side of the figure. Similarly, since the azimuthal separation between the GOES 15 and 12 pair is about 30°, the resolved m range is only [-6, 6] in panel (e2). Even though the GOES 15 and 12 pair cannot cover as high m values as the GOES 13 and

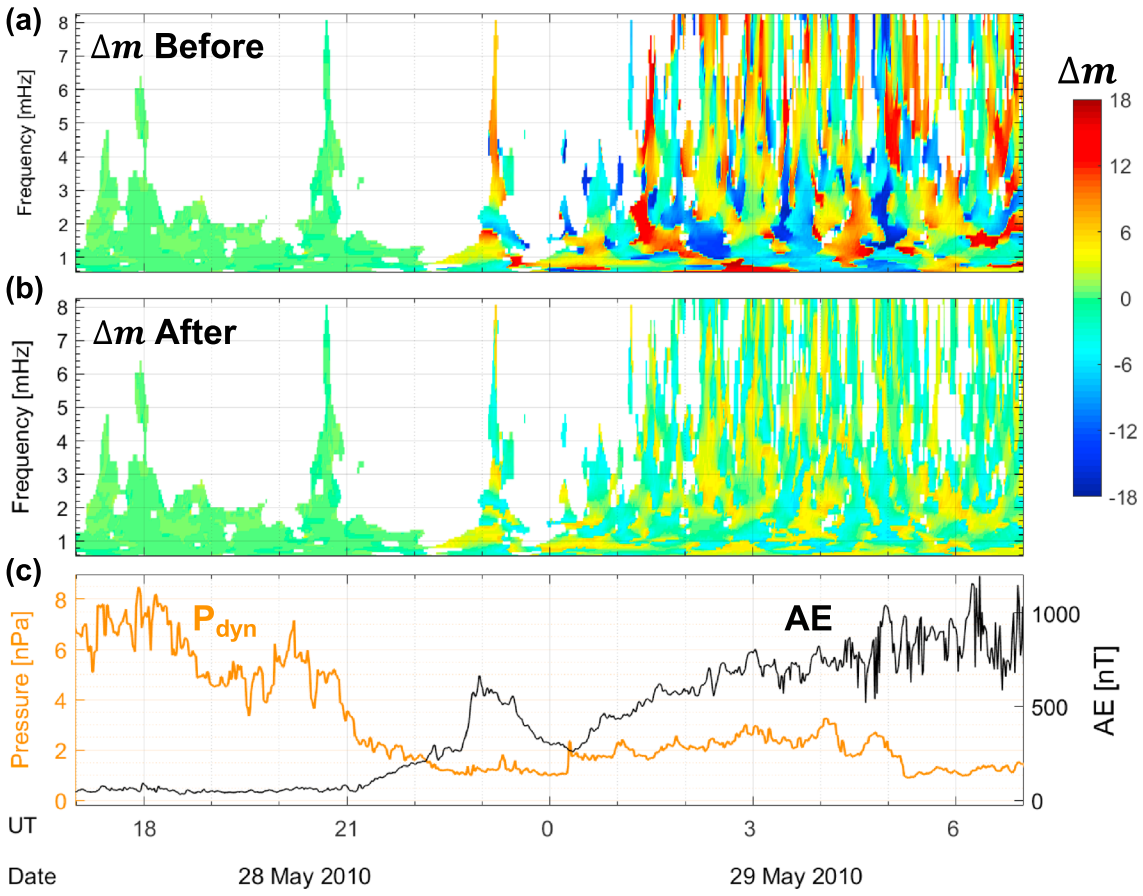

Figure 9. (a and b) The difference in the resolved mode number between two pairs of GOES 13 and 12 and GOES 15 and 12 before and after the cross-pair analysis. (c) Solar wind dynamic pressure P_{dyn} and AE index for the interval.

12 pair, the mode results in the overlapping m range between the two pairs should be generally consistent. This is true for the high solar wind P_{dyn} interval (17-22UT of 28 May), showing dominant integrated wave power at low modes summed over m = 1 to 3 (blue curve), which is consistent between two pairs. However, for the subsequent high AE interval, at many times the mode distributions become inconsistent between the two pairs, especially at high-mode numbers (the green curves). For example, at 5UT of 29 May, the GOES 15 and 12 pair in panel (e2) shows a high power in the m range of $4 \leq |m| \leq 6$ (solid and dashed green curves), while the GOES 13 and 12 pair in panel (e1) shows a peak of power in the m range of [-12, -10] (dashed magenta curve). To further illustrate the different results from the two pairs, in Figure 9a we plot the difference in the resolved m number (Δm) between the two pairs at each time and frequency. Green means good agreement between two pairs, while red and blue indicate large disagreement. Consistent with the results of Figures 8e1 and 8e2, we see persistent good agreement between two pairs during the high P_{dyn} interval over all frequencies, but large disagreement up to $|\Delta m|$ ~18 appears frequently during the high AE interval.

The mismatch between the two pairs during the high AE interval could be due to the $2n\pi$ ambiguity in the resolved X-Phase. In the XWT analysis, the X-Phase range is defined to be [-180°, 180°], which is sufficient to resolve the low-mode structures given the ~15° azimuthal separation between the GOES 13 and 12 pair and even the ~30° separation between the GOES 15 and 12 pair. This explains why during the high P_{dyn} interval when the low modes are dominant, the two pairs show consistent mode distributions from XWT analysis. However, the [-180°, 180°] range may not be sufficient to cover the high-mode numbers during the high AE interval. Yet due to the $2n\pi$ ambiguity in the XWT analysis, the X-Phase cannot be uniquely determined. Here we reduce the ambiguity in the phase difference and thus the mode number by comparing and reconciling the mode numbers between the two overlapping pairs. Specifically, for each pair and at each time and

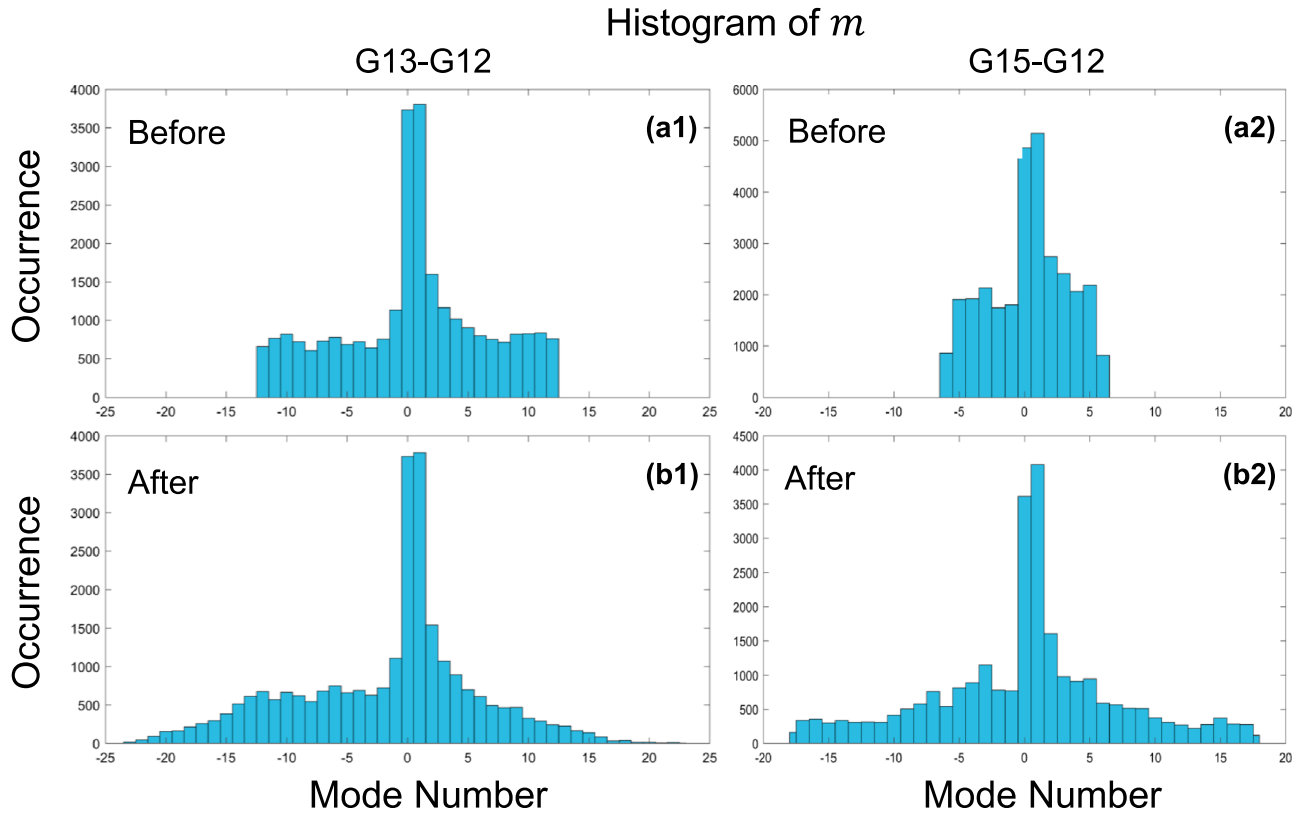

Figure 10. Histograms of the mode numbers at different times and frequencies during the same period as Figure 9. (a1 and b1) Before and after the cross-pair analysis respectively for the GOES 13 and 12 pair. (a2 and b2) Before and after the analysis for the GOES 15 and 12 pair.

frequency (e.g., Figure 8d1), we allow the phase difference to be three possible values, X-Phase−360°, X-Phase, and X-Phase+360°, where X-Phase is the phase difference directly from the XWT analysis in the range of [-180°, 180°]. Correspondingly, three possible values of mode number $m1$ are calculated using equation (1) for pair 1 (GOES 13 and 12) at each frequency-time bin, and the same for m2 of pair 2 (GOES 15 and 12). Then for each time and frequency, we cross compare the possible mode values from each pair to find the $m1$ from pair 1 that is the closest to the $m2$ from pair 2, that is, $|\Delta m| = |m1 - m2|$reaching a minimum. As a result, the mode numbers, $m1$ and $m2$, that produce the minimum difference are used as the final and more realistic mode numbers for the two pairs.

After performing this cross-pair analysis, Figure 9b shows the new results of the mode number difference Δm between two pairs. We see that the mode difference is mostly within the range of $|\Delta m| < 6$ (green or yellow colors), illustrating a significant improvement over Figure 9a before the analysis. A new comparison of the integrated wave power at different mode ranges is also shown in Figures 8f1 and 8f2 after the cross-pair analysis. First, we see that with the new analysis, both pairs can resolve waves at higher mode numbers (e.g., the new red curves with $|m| \geq 13$), the power of which comes from the waves previously at lower mode numbers before applying the cross-pair analysis. For example, for the GOES 15 and 12 pair we find that from Figures 8e2 before the cross-pair analysis to 8(f2) after the new analysis, the power in the range of $4 \leq |m| \leq 6$ (solid and dashed green curves) generally decreases, which is actually converted to the power at $|m| \geq 13$ (red curves). More importantly, by comparing the new power distributions after the cross-pair analysis between the two pairs (Figures 8), we find that the distributions of wave power at different mode number ranges (different colors) reach a better agreement between the two pairs. Furthermore, we compare the histograms of the mode number before and after the cross-pair analysis for each pair in Figure 10. The mode numbers resolved at all the times and frequencies during the entire period of Figure 9 are included in the histogram analysis. X axes are the mode number m values, and the y axes show the counts of the time-frequency bins possessing the corresponding m values. Panel (a1) of Figure 10 is for the GOES 13 and 12

pair before the cross-pair analysis, and panel (a2) is after, similar for panels (a2) and (b2), which are before and after the analysis for the GOES 15 and 12 pair. Again, before the cross-pair analysis, the resolved mode numbers for the GOES 13 and 12 pair is confined in the range of [-12, 12] (panel (a1)) and for the GOES 15 and 12 pair is in the range of [-6, 6] (panel (a2)). Both distributions show sharp cuts at the maximum and minimum mode numbers that can be resolved by the XWT analysis. The distributions are also inconsistent between the two pairs before performing the cross-pair analysis. However, after the cross-pair analysis, in panels (b1) and (b2), we find that the mode numbers can reach higher ($\pm$24 for GOES 13 and 12 pair and $\pm$18 for GOES 15 and 12 pair) values and histograms show a more gradual drop as $|m|$ increases, which is consistent with the physical nature of ULF pulsations. In addition, the histograms after the analysis show a better agreement between the two pairs (panels (b1) versus (b2)). Therefore, the improved agreement of mode number distributions between the two pairs (Figures 8–10) and the more realistic distributions of mode number (the histograms) demonstrate that the cross-pair analysis is efficient in reducing the $2n\pi$ ambiguity in the phase difference and generating more reliable mode numbers during the high AE interval when the contribution from high-mode numbers is significant.

6. Discussion and Conclusions

To understand and quantify the radial diffusion process in Earth's radiation belts, a reliable estimation of the azimuthal mode structure of ULF waves is required. In this paper, we quantify the azimuthal mode numbers of the compressional Pc5 ULF waves based on multiple pairs of GOES satellite observations. The 28-31 May 2010 geomagnetic storm is selected for the study since we have five GOES satellites available during this time, which provide a wide range of local time coverage at the same time. In addition, the storm includes distinct intervals with either high solar wind dynamic pressure (P_{dyn})-low AE activity or low P_{dyn}-high AE, which may correlate with different ULF wave structures. A cross-spectral technique, XWT, is applied to each pair, and by combining the results from multiple pairs, temporal and spatial variations of the ULF wave mode structure during the storm are resolved. The work also makes improvements over many previous works (e.g., Li et al., 2016; Sarris, 2014; Sarris et al., 2013; Sarris & Li, 2017) by including both positive and negative mode numbers in the analysis (i.e., waves propagating in both eastward and westward directions) and by reducing the $2n\pi$ ambiguity in the cross-spectral analysis, both of which contribute to more reliable mode number estimations. The specific results and conclusions are summarized below.

During the storm commencement, when the solar wind P_{dyn} is high while AE is low, the XWT results show that the ULF wave power is mostly dominated by low-mode numbers ($m = 1$ or -1), which is consistent with previous studies (e g., Sarris & Li, 2017; Tu et al., 2012). Our results suggest that these low-mode ULF waves are probably driven by large-scale solar wind dynamic pressure variations on the dayside (e.g., Hughes, 1994; Olson & Rostoker, 1978), based on the strong correlation between the appearance of the low-mode wave structure and the enhanced solar wind P_{dyn} in Figure 5. Another possible driver of low-mode ULF wave is Kelvin-Helmholtz instability as a result of high-speed solar wind (e.g., Mann et al., 1999). However, the solar wind conditions in Figure 1 show that the solar wind speed remains elevated when the P_{dyn} drops, thus not well correlated with the low-mode wave structure in Figure 5. This indicates that Kelvin-Helmholtz instability is less likely to be the main driver for the low-mode ULF waves during this event. Furthermore, we find that if only positive mode numbers are allowed, similar to some previous studies (e g. Li et al., 2016; Sarris, 2014; Sarris et al., 2013), the mode structure becomes unrealistic during the high P_{dyn} interval, which suggests that allowing for both positive and negative mode numbers is critical in the analysis. Accurately resolving the sign of mode number is important to precisely quantify the radial diffusion coefficient, D_{LL}. During the high P_{dyn} period, an interesting change of sign in mode number, m, occurs in the slightly prenoon region (around 9.5-10.5 hr MLT). After comparing the MLT distributions of the mode structure from multiple pairs of GOES satellites, we have confirmed that this sign change of m is spatial rather than temporal, with eastward propagation in the noon to dusk sector and westward propagation in the noon to dawn sector. This is consistent with compressional ULF waves externally driven by high-pressure solar wind buffeting around noon, creating antisunward propagation of waves on both sides (e.g., Hughes, 1994; Olson & Rostoker, 1978). Furthermore, using the wide MLT coverage of the multiple pairs of GOES satellites at the same time, we find that the low-mode ULF waves may not be as global as previously assumed, limited to regions

away from midnight. This limited local time extent of the low-mode structure needs to be properly considered in the calculation of D_{LL} for energetic particles.

In contrast, during the storm main phase and early recovery phase when the solar wind P_{dyn} is low and AE is high, the XWT results show that the wave power spreads almost evenly over all different mode numbers from low to high. The strong correlation between the appearance of the high-mode ULF waves and high AE in Figure 5 suggests that these waves may be driven by small-scale substorm injections from the nightside (e.g., James et al., 2013; Yeoman et al., 2010). By investigating the MLT-distribution of the mode structure during the high AE period from multiple pairs of GOES satellites, we find that the evenly distributed mode structure or the significant contribution from high modes is not limited to localized regions close to midnight, as generally assumed, and can spread all the way to the MLT regions on the dayside. Possible mechanisms for high-mode ULF waves near the dayside region include a wave-particle source mechanism involving drift-mirror instabilities (e.g., Walker et al., 1982; Yeoman et al., 1992) and a dispersive waveguide model with the high-m waves propagating both sunward and antisunward from the sources at flank regions (Fenrich et al., 1995). More detailed wave and particle analysis is needed in the future to resolve the driving mechanism during this event. This more global local time coverage of the evenly distributed mode structure up to high modes also needs to be considered realistically in D_{LL} calculations.

Furthermore, to reduce the $2n\pi$ ambiguity in the resolved phase difference from the XWT analysis, a cross-pair analysis is performed on satellite field measurements here for the first time over two pairs of GOES satellites that overlap azimuthally. First, the XWT results from the two pairs suggest that a cross-pair analysis is necessary for the high AE intervals when the resolved mode numbers can be largely inconsistent. Then after comparing and reconciling the mode number results from the two pairs using the cross-pair analysis, the mode structures from the two pairs show a significantly improved agreement. These results demonstrate that the analysis is efficient in reducing the $2n\pi$ ambiguity and generating reliable mode structure during the high AE interval when the mode numbers can be high. In section 5 the cross-pair analysis has only been applied as a proof of concept to the selected interval of the event. If applying to the entire event, we would expect that the low-mode-dominated results in Figures 5 and 6 during high P_{dyn} (and low AE) times remain mostly unchanged, while the detailed mode fraction results during high AE times in Figures 5 and 7 show changes similar to the high AE interval analyzed in section 5. Applying this cross-pair analysis to the entire event interval will be an important part of our future work. Additionally, in the cross-pair analysis, we only added one full phase period to both directions of the phase difference (i.e., $\pm 2\pi$) since our results show that this is sufficient to reach a good agreement between the pairs and to achieve accurate distributions of the mode numbers (e.g., the histograms in Figures 10b1 and 10b2). This could be due to the fact that the contribution of even higher mode numbers ($m \geq 25$ in the histograms) is insignificant for this period. Even though a better agreement is reached, the mode structures are still not identical between the pairs. To further improve the results, the cross-pair analysis needs to be applied to more overlapping pairs (e.g., three pairs with small azimuthal separation rather than two) to cross-compare and reconcile the resolved mode structures.

Similar cross-pair analysis has been performed on ground-based ULF wave measurements in previous works (e.g., Baker et al., 2003; Chisham & Mann, 1999), but there are differences between our approaches. For instance, Chisham and Mann (1999) used three ground magnetometer pairs two of which are not overlapping, while here we only use the overlapping pairs (GOES13-12 and GOES 15-12) to better ensure they are measuring the same ULF wave. Additionally, in Chisham and Mann (1999) the sign of m is resolved by analyzing the arrival time of the waveform, while in our approach we let the sign of m be part of the comparison and choose m with the minimum difference between two pairs. Last but not least, our cross-pair analysis is performed on ULF waves measured in space while the analysis in Chisham and Mann (1999) is performed on ground magnetometers, which makes estimating $m>50$ nominally impossible due to the ionospheric screening.

The analysis presented in this work needs also to be applied to more case studies with different drivers of solar wind and geomagnetic conditions. In addition to multiple GOES satellites, the analysis can also be conducted for other space missions including National Aeronautics and Space Administration (NASA) Van Allen Probes, THEMIS (Time History of Events and Macroscale Interactions during Substorms), and MMS (Magnetospheric Multiscale) missions to resolve the mode structure at a wide range of L shells and

local times. With the electric field measurements from these other missions, similar analysis from this paper can be applied to study the mode structure of poloidal and toroidal ULF waves. In addition, the MMS mission is best suited due to the close separation between the satellites (as small as tens of kilometers), making it possible to resolve very high-mode numbers (order of hundreds; e.g., Le et al., 2017; Murphy et al., 2018). With a good database of the ULF mode numbers at different solar wind and geomagnetic conditions, we can construct statistical maps of mode structures under different driving conditions, which will be directly useful in quantifying the radial diffusion process in Earth's inner magnetosphere and in resolving its contribution to the overall dynamics of energetic particles.

Acknowledgments
This work was supported by NSF grant AGS 1752736 and NASA grants NNX16AG71G and 80NSSC18K1284. The authors would like to thank NOAA for providing high-quality magnetic field observations from the GOES spacecraft. The authors thank Goddard Space Flight Center, Space Flight Data Facility of NASA for providing the SSC 4D Orbit Viewer 4.2.7 software for visualization of the GOES satellite orbits. The authors are grateful for thoughtful discussions with Mary Hudson. Data used in the paper are deposited on the data repository of the Department of Physics and Astronomy at West Virginia University with link https://ulysses.phys.wvu.edu/plasma/?q=node/214, which is publicly available.

References

Ali, A. F., Elkington, S. R., Tu, W., Ozeke, L. G., Chan, A. A., & Friedel, R. H. W. (2015). Magnetic field power spectra and magnetic radial diffusion coefficients using CRRES magnetometer data. *Journal of Geophysical Research: Space Physics*, *120*, 973–995. https://doi.org/10.1002/2014JA020419

Baker, G., Donovan, E. F., & Jackel, B. J. (2003). A comprehensive survey of auroral latitude Pc5 pulsation characteristics. *Journal of Geophysical Research*, *108*(A10), 1384. https://doi.org/10.1029/2002JA009801

Brautigam, D. H., Ginet, G. P., Albert, J. M., Wygant, J. R., Rowland, D. E., Ling, A., & Bass, J. (2005). CRRES electric field power spectra and radial diffusion coefficients. *Journal of Geophysical Research*, *110*(A2), A02214. https://doi.org/10.1029/2004JA010612

Chisham, G., & Mann, I. R. (1999). A Pc5 ULF wave with large azimuthal wavenumber observed within the morning sector plasmasphere by Sub-Auroral Magnetometer Network. *Journal of Geophysical Research*, *104*(A7), 14,717–14,727. https://doi.org/10.1029/1999JA900147

Elkington, S. R., Hudson, M. K., & Chan, A. A. (1999). Acceleration of relativistic electrons via drift-resonant interaction with toroidal-mode Pc-5 ULF oscillations. *Geophysical Research Letters*, *26*(21), 3273–3276. https://doi.org/10.1029/1999GL003659

Elkington, S. R., Hudson, M. K., & Chan, A. A. (2003). Resonant acceleration and diffusion of outer zone electrons in an asymmetric geomagnetic field. *Journal of Geophysical Research*, *108*(A3), 1116. https://doi.org/10.1029/2001JA009202

Eriksson, A. I. (1998). Spectral analysis. In G. Paschmann & P. W. Daly (Eds.), *Multi-spacecraft analysis methods revisited*, edited by, *SR-001 in ISSI Scientific Reports* (Chap. 1, pp. 5–43). Noordwijk, Netherlands: ESA Publications Division.

Fälthammar, C.-G. (1965). Effects of time-dependent electric fields on geomagnetically trapped radiation. *Journal of Geophysical Research*, *70*(11), 2503–2516. https://doi.org/10.1029/JZ070i011p02503

Fei, Y., Chan, A. A., Elkington, S. R., & Wiltberger, M. J. (2006). Radial diffusion and MHD-particle simulations of relativistic electron transport by ULF waves in the September 1998 storm. *Journal of Geophysical Research*, *111*(A12), A12209. https://doi.org/10.1029/2005JA011211

Fenrich, F. R., Samson, J. C., Sofko, G., & Greenwald, R. A. (1995). ULF high- and low m field line resonances observed with the Super Dual Auroral Radar Network. *Journal of Geophysical Research*, *100*(A11), 21,535–21,547. https://doi.org/10.1029/95JA02024

Grinsted, A., Moore, J. C., & Jevrejeva, S. (2004). Application of the cross wavelet transform and wavelet coherence to geophysical time series. *Nonlinear Processes in Geophysics*, *11*(5/6), 561–566. https://doi.org/10.5194/npg-11-561-2004

Hughes, W. J. (1994). Magnetospheric ULF waves: A tutorial with a historical perspective. In M. J. Engebretson, K. Takahashi, & M. Scholer (Eds.), *Solar wind sources of magnetospheric ultra-low-frequency waves* (Chap. 1, pp. 1–11). Washington, DC: American Geophysical Union. https://doi.org/10.1029/GM081p0001

James, M. K., Yeoman, T. K., Mager, P. N., & Klimushkin, D. Y. (2013). The spatio-temporal characteristics of ULF waves driven by substorm injected particles. *Journal of Geophysical Research: Space Physics*, *118*, 1737–1749. https://doi.org/10.1002/jgra.50131

Kellogg, P. J. (1959). Van Allen radiation of solar origin. *Nature*, *183*(4671), 1295–1297. https://doi.org/10.1038/1831295a0

Kivelson, M. G., & Russel, C. T. (1995). *Introduction to space physics* (Chap. 11, pp. 330–354). Cambridge, UK: Cambridge University Press.

Le, G., Chi, P. J., Strangeway, R. J., Russell, C. T., Slavin, J. A., Takahashi, K., et al. (2017). Global observations of magnetospheric high-m poloidal waves during the 22 June 2015 magnetic storm. *Geophysical Research Letters*, *44*, 3456–3464. https://doi.org/10.1002/2017GL073048

Li, Z., Hudson, M., Paral, J., Wiltberger, M., & Turner, D. (2016). Global ULF wave analysis of radial diffusion coefficients using a global MHD model for the 17 March 2015 storm. *Journal of Geophysical Research: Space Physics*, *121*, 6196–6206. https://doi.org/10.1002/2016JA022508

Li, Z., Hudson, M., Patel, M., Wiltberger, M., Boyd, A., & Turner, D. (2017). ULF wave analysis and radial diffusion calculation using a global MHD model for the 17 March 2013 and 2015 storms. *Journal of Geophysical Research: Space Physics*, *122*, 7353–7363. https://doi.org/10.1002/2016JA023846

Loto'aniu, T. M., Mann, I. R., Ozeke, L. G., Chan, A. A., Dent, Z. C., & Milling, D. K. (2006). Radial diffusion of relativistic electrons into the radiation belt slot region during the 2003 Halloween geomagnetic storms. *Journal of Geophysical Research*, *111*(A4), A04218. https://doi.org/10.1029/2005JA011355

Mann, I. R., Chisham, G., & Bale, S. D. (1998). Multisatellite and ground-based observations of a tailward propagating Pc5 magnetospheric waveguide mode. *Journal of Geophysical Research*, *103*(A3), 4657–4669. https://doi.org/10.1029/97JA03175

Mann, I. R., Lee, E. A., Claudepierre, S. G., Fennell, J. F., Degeling, A., Rae, I. J., et al. (2013). Discovery of the action of a geophysical synchrotron in the Earth's Van Allen radiation belts. *Nature Communications*, *4*(1), 1–6. https://doi.org/10.1038/ncomms3795

Mann, I. R., Wright, A. N., Mills, K. J., & Nakariakov, V. M. (1999). Excitation of magnetospheric waveguide modes by magnetosheath flows. *Journal of Geophysical Research*, *104*(A1), 333–353. https://doi.org/10.1029/1998JA900026

Murphy, K. R., Inglis, A. R., Sibeck, D. G., Rae, I. J., Watt, C. E. J., Silveira, M., et al. (2018). Determining the mode, frequency, and azimuthal wave number of ULF waves during a HSS and moderate geomagnetic storm. *Journal of Geophysical Research: Space Physics*, *123*(8), 6457–6477. https://doi.org/10.1029/2017JA024877

Nishida, A. (1978). *Geomagnetic diagnosis of the magnetosphere* (p. 256). New York: Springer. https://doi.org/10.1007/978-3-642-86825-2

Olson, J. V., & Rostoker, G. (1978). Longitudinal phase variations of Pc 4-5 micropulsations. *Journal of Geophysical Research*, *83*(A6), 2481–2488. https://doi.org/10.1029/JA083iA06p02481

Perry, K. L., Hudson, M. K., & Elkington, S. R. (2005). Incorporating spectral characteristics of Pc5 waves into three-dimensional radiation belt modeling and the diffusion of relativistic electrons. *Journal of Geophysical Research*, *110*(A3), 215. https://doi.org/10.1029/2004JA010760

Rioul, O., & Vetterli, M. (1991). Wavelets and signal processing. *IEEE Signal Processing Magazine*, *8*(4), 14–38. https://doi.org/10.1109/79.91217

Roederer, J. G. (1970). *Dynamics of geomagnetically trapped radiation*. New York: Springer. https://doi.org/10.1007/978-3-642-49300-3

Sarris, T. E. (2014). Estimates of the power per mode number of broadband ULF waves at geosynchronous orbit. *Journal of Geophysical Research: Space Physics*, *119*, 5539–5550. https://doi.org/10.1002/2013JA019238

Sarris, T. E., & Li, X. (2017). Geomagnetic activity and local time dependence of the distribution of ultra low-frequency wave power in azimuthal wavenumbers, *m*. *Annales de Geophysique*, *35*(3), 629–638. https://doi.org/10.5194/angeo-35-629-2017

Sarris, T. E., Li, X., Liu, W., Argyriadis, E., Boudouridis, A., & Ergun, R. (2013). Mode number calculations of ULF field-line resonances using ground magnetometers and THEMIS measurements. *Journal of Geophysical Research: Space Physics*, *118*, 6986–6997. https://doi.org/10.1002/2012JA018307

Sarris, T. E., Li, X., & Temerin, M. (2006). Simulating radial diffusion of energetic (MeV) electrons through a model of fluctuating electric and magnetic fields. *Annales de Geophysique*, *24*(10), 2583–2598. https://doi.org/10.5194/angeo-24-2583-2006

Sarris, T. E., Liu, W., Kabin, K., Li, X., Elkington, S. R., Ergun, R., et al. (2009). Characterization of ULF pulsations by THEMIS. *Geophysical Research Letters*, *36*, L04104. https://doi.org/10.1029/2008GL036732

Schulz, M., & Lanzerotti, L. J. (1974). *Particle diffusion in the radiation belts, Physics and Chemistry in Space* (Vol. 7). New York: Springer-Verlag. https://doi.org/10.1007/978-3-642-65675-0

Shi, X., Baker, J. B. H., Ruohoniemi, J. M., Hartinger, M. D., Murphy, K. R., Rodriguez, J. V., et al. (2018). Long-lasting poloidal ULF waves observed by multiple satellites and high-latitude SuperDARN radars. *Journal of Geophysical Research: Space Physics*, *123*(10), 8422–8438. https://doi.org/10.1029/2018JA026003

Takahashi, K., Claudepierre, S. G., Rankin, R., Mann, I. R., & Smith, C. W. (2018). Van Allen Probes observation of a fundamental poloidal standing Alfvén wave event related to giant pulsations. *Journal of Geophysical Research: Space Physics*, *123*(6), 4574–4593. https://doi.org/10.1029/2017JA025139

Takahashi, K., Hartinger, M. D., Angelopoulos, V., Glassmeier, K.-H., & Singer, H. J. (2013). Multispacecraft observations of fundamental poloidal waves without ground magnetic signatures. *Journal of Geophysical Research: Space Physics*, *118*, 4319–4334. https://doi.org/10.1002/jgra.50405

Takahashi, K., McEntire, R. W., Lui, A. T. Y., & Potemra, T. A. (1990). Ion flux oscillations associated with a radially polarized transverse Pc 5 magnetic pulsation. *Journal of Geophysical Research*, *95*(A4), 3717–3731. https://doi.org/10.1029/JA095iA04p03717

Torrence, C., & Compo, G. P. (1998). A practical guide to wavelet analysis. *Bulletin of the American Meteorological Society*, *79*(1), 61–78. https://doi.org/10.1175/1520-0477(1998)079<0061:APGTWA>2.0.CO;2

Tu, W., Elkington, S. R., Li, X., Liu, W., & Bonnell, J. (2012). Quantifying radial diffusion coefficients of radiation belt electrons based on global MHD simulation and spacecraft measurements. *Journal of Geophysical Research*, *117*(A10), A10210. https://doi.org/10.1029/2012JA017901

Walker, A. D. M., Greenwald, R. A., Korth, A., & Kremser, G. (1982). STARE and GEOS 2 observations of a storm time Pc 5 pulsation. *Journal of Geophysical Research*, *87*(A11), 9135. https://doi.org/10.1029/JA087iA11p09135

Yeoman, T. K., Klimushkin, D. Y., & Mager, P. N. (2010). Intermediate-m ULF waves generated by substorm injection: A case study. *Annales de Geophysique*, *28*(8), 1499–1509. https://doi.org/10.5194/angeo-28-1499-2010

Yeoman, T. K., Tian, M., Lester, M., & Jones, T. B. (1992). A study of Pc 5 hydromagnetic waves with equatorward phase propagation. *Planetary and Space Science*, *40*(6), 797–810. https://doi.org/10.1016/0032-0633(92)90108-Z

Zong, Q.-G., Rankin, R., & Zhou, X. (2017). The interaction of ultra-low-frequency pc3-5 waves with charged particles in Earth's magnetosphere. *Reviews of Modern Plasma Physics*, *1*(1), 10. https://doi.org/10.1007/s41614-017-0011-4

Zong, Q.-G., Zhou, X. Z., Li, X., Song, P., Fu, S. Y., Baker, D. N., et al. (2007). Ultralow frequency modulation of energetic particles in the dayside magnetosphere. *Geophysical Research Letters*, *34*, L12105. https://doi.org/10.1029/2007GL029915

Erratum

In the originally published version of this article, the table headers appearing the first row of Figure 2b were missing. The error has since been corrected and this version may be considered the authoritative version of record. The update to the figure appears only in the electronic version of the article, not in the PDF.